Chinese Chemical Letters 34 (2023) 108538

Contents lists available at ScienceDirect

Chinese Chemical Letters

journal homepage: www.elsevier.com/locate/cclet

Interfacial self-transportation *via* controlled wettability transition for directed self-assembly

Pan Tian, Minghui Tan, Guiqiang Zhu, Dan Wang, Guoxin Lu, Mengjiao Cheng*

State Key Laboratory of Chemical Resource Engineering & Beijing Laboratory of Biomedical Materials & Beijing Advanced Innovation Centre for Soft Matter Science and Engineering, Beijing University of Chemical Technology, Beijing 100029, China

ARTICLE INFO

Article history:
Received 18 January 2023
Revised 6 May 2023
Accepted 6 May 2023
Available online 8 May 2023

Keywords:
Wettability transition
Tracks
Capillary force
Self-transportation
Directed self-assembly

ABSTRACT

Wettability transition is a significant responsive mechanism which is widely applied to construct smart materials and systems. The broad-spectrum responsiveness of the wettability transition makes it a promising way to expand innovative applications. Here, we develop a track-guided self-transportation system mediated by sequential wettability transition accompanied with capillary transportation. Alkaline fuel is loaded into polydimethylsiloxane (PDMS) cuboid to trigger the wettability transition of distributed superhydrophobic tracks laid in shallow water. After the wettability transition, the induced capillary force can propel the repetitive track-to-track transportation of PDMS. Importantly, the spacing between adjacent tracks is rationally designed based on multiple factors including threshold of wettability transition, diffusion kinetics and capillary interaction. Furthermore, the track-guided transportation system is applied to realize directed self-assembly of multiple PDMS building blocks for designated configuration, which increases the complexity and intelligence of self-assembly systems.

The scientific community has long been attracted by surfaces with wettability transition owing to the significant superiority in functional integration and environmental interaction [1–3]. Early in 2003, Langer *et al.* [4] applied electrical potential to induce the conformational transitions of a monolayer of (16-mercapto) hexadecanoic acid on a gold surface, and thus the surface underwent a transition from a hydrophilic state to a moderately hydrophobic one. Then in 2004, Jiang *et al.* [5] extended the range of wettability transition from superhydrophobicity to superhydrophilicity by constructing aligned nanorod arrays on UV-sensitive ZnO films. Furthermore, they realized reversible wettability transition by grafting in the copolymer films of P(NIPAAm-*co*-AAc) owing to the switch of the copolymer chain conformations in response to both temperature and pH changes [6]. The above pioneering reports have demonstrated the universal design principle of stimuli-responsive surfaces with wettability transition, namely, regulating both the chemical compositions and micro-nano hierarchical structures of the surfaces [7–9].

Until now, a variety of environmental stimuli have been applied to achieve responsive wettability transition, including light irradiation [10–12], temperature [13,14], magnetic field [15], electric field [16,17], stress [18] or specific pH environment [19,20]. Accordingly, wettability transition surfaces have benefited diverse applications, such as on-demand oil/water (or emulsion) separation [21,22], intelligent microfluidic gate [23], droplet manipulation [24], and controllable device propulsion [25,26]. For example, Feng *et al.* [27] applied a patterned surface with anisotropic wettability transition to explore the application in real-time detection with visible signals during oil/water separation. Hou *et al.* [28] tuned the wettability of pore structures in a porous matrix, to regulate the bubble size for the use of efficient and continuous air purification. These advanced applications have demonstrated the prospect of surfaces with the property of wettability transition. Yet, new applicable scenarios remain to be explored to advance the intelligence of such smart surfaces, which exhibit the trend in high integration of multiple functions and more tasks with complex features [29,30].

To advance the intelligence of stimulus-responsive surfaces in new applications, herein, we have demonstrated a track-guided self-transportation system by coordinating multiple dynamic processes including wettability transition, capillary interaction, and controlled release of chemical fuel. Specifically, the system consists of two components: (I) a polydimethylsiloxane (PDMS) cuboid loaded with an alkaline 'fuel' of pressed $NaOH/Na_2CO_3$ powders to be continuously released; the four side surfaces of the PDMS cuboid were modified with alternate wettability of superhydrophobic-superhydrophilic (Figs. 1a and b, Fig. S1 in Supporting information); (II) pre-laid tracks with pH-responsive wet-

* Corresponding author.
E-mail address: chengmj@mail.buct.edu.cn (M. Cheng).

https://doi.org/10.1016/j.cclet.2023.108538
1001-8417/

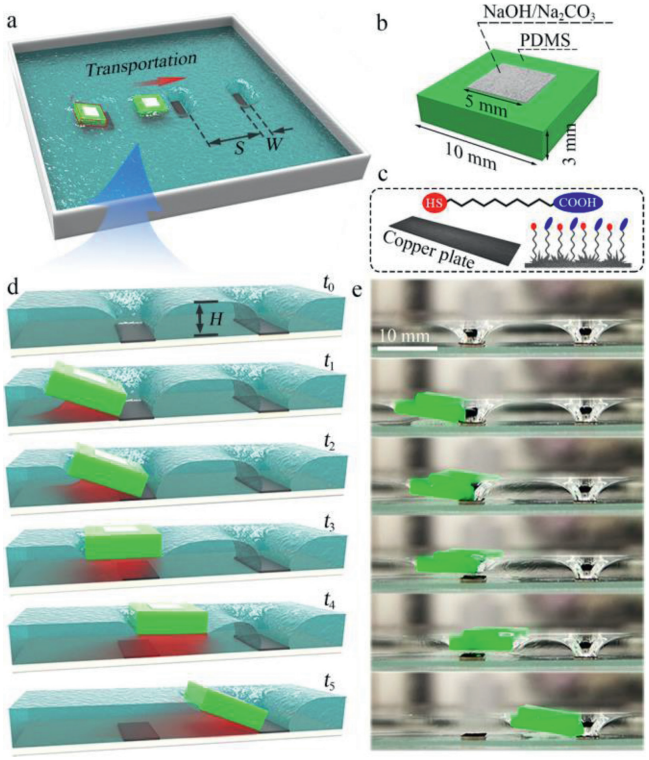

Fig. 1. (a) Schematic illustration of PDMS transportation at an air/water interface by laying tracks. (b) Design of PDMS cuboid. (c) Copper plates with a thiol coating are used as pH-responsive tracks. (d) Stepwise transportation of PDMS. (e) Side-view snapshots displaying the transportation of PDMS.

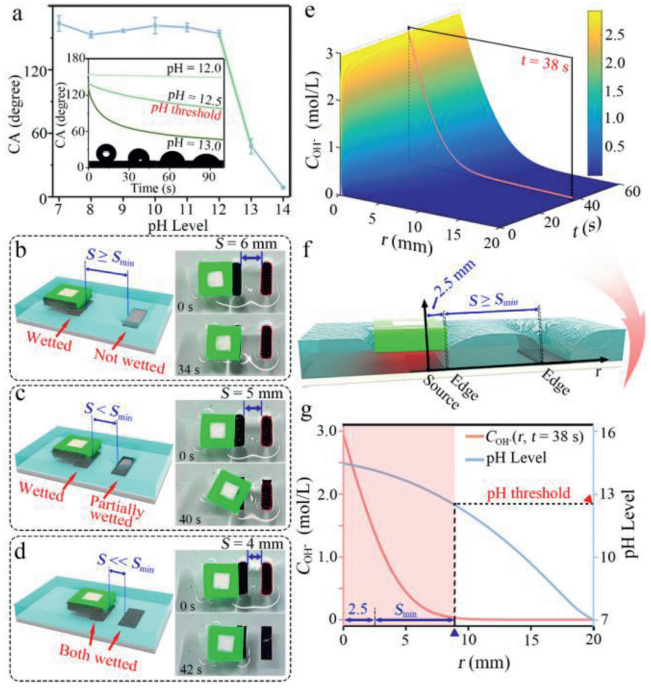

Fig. 2. (a) CAs of tracks with different pH; insets: time-dependent CA changes and the snapshots displaying CA changes (pH 12.5) at 0 s, 60 s, 120 s, and 500 s. (b-d) S_{min} obtained by gradually adjusting the track spacing. (e) Simulated $C_{(OH^-)}$ (r, t) from the alkaline release point to increased diffusion distance and time. (f) Illustration of S_{min}. (g) Distance-dependent changes of $C_{(OH^-)}$ (r, $t = 38$ s) and the pH gradient in the aquatic environment.

tability transition from superhydrophobic (neutral conditions) to superhydrophilic (alkaline conditions) (Fig. 1c and Fig. S2 in Supporting information); these tracks were prepared by deposition of copper plates in a $HAuCl_4$ solution and subsequent surface modification of a layer of $HS(CH_2)_{10}COOH$.

A complete track-to-track transportation process is displayed in Figs. 1d and e, and Video S1 (Supporting information). We pre-laid the as-prepared tracks at the bottom of the container with a thin layer (the water height, $H = 3.0$ mm; Fig. S3 in Supporting information). Negative menisci were observed around the tracks due to the superhydrophobicity. Then, from the moment t_0 to t_1, the hydrophobic PDMS was attracted to the edge of the nearest track *via* the hydrophobic capillary attraction [31,32] between its side surface and the track. With the simultaneous release and diffusion of alkaline 'fuel', the increased local pH caused the gradual wettability transition of the track. The dynamic transition process was visualized and demonstrated by observing the migration of the three-phase contacting line (Video S2 in Supporting information): When we injected an alkaline solution with a syringe on the left side of the track to simulate the diffusion of the alkaline fuel loaded on PDMS, we observed the clear migration and deformation of the menisci upon the alkaline solution reaching the edge of the track; the menisci around the edge of the track disappeared suddenly within 16 ms to complete the wettability transition (from t_2 to t_3). Accordingly, the PDMS was 'freed' to float (at the moment t_3) and its right-side meniscus merged with that of the next superhydrophobic track. As a result, the asymmetric menisci of the opposite side surfaces created a net lateral force to propel the PDMS for the directional transportation from track to track (from t_3 to t_5). The underlying mechanism of this capillary transportation is similar to the phenomenon of buoyant seeds being drawn to aquatic plants, *i.e.*, the principle of minimizing the interfacial free energy [33]. When the PDMS reached the next track, a new cycle of wettability transition and capillary transportation started, thus realizing the long-range track-to-track transportation.

One vital factor to achieve the above track-to-track transportation is to ensure the selective wettability transition of the nearest track that traps the PDMS while other distant tracks remain superhydrophobic; otherwise, the transportation would be interrupted. Therefore, we determined the pH threshold to trigger the wettability transition by studying the pH-dependent water contact angle (CA) changes of the as-prepared tracks. The results (Fig. 2a) display a threshold of pH 12.5, below which the tracks keep superhydrophobic. When pH > 12.5, the surfaces turned from superhydrophobicity to superhydrophilicity gradually. Because the local pH values decay with the increasing diffusion distance of the alkaline 'fuel', it is possible to realize selective wettability transition of designated tracks even in the same aquatic system by taking advantage of the pH gradient. Specifically, the minimum track spacing (S_{min}) exists, below which two adjacent tracks would be both wetted as the local pH value exceeds the threshold. Only when the spacing of two adjacent tracks larger than S_{min}, selective wetting of one track that is nearer to the diffusion point is possible.

Hence, to measure the S_{min}, we have varied the track spacing and observed the wetting states of the next track when the wettability transition of the first track was completed. When the track spacing (S) was larger than or equal to S_{min}, the local pH value near the next track decayed to a level lower than the pH threshold, and thus made it unwetted. We found the critical track spacing of 6 mm (Fig. 2b and Video S3 in Supporting information), under which selective wettability transition was realized. When the spacing was lower than S_{min}, the neighboring track was partially wetted ($S = 5$ mm, Fig. 2c), because the local pH value around the neighboring track was above the threshold to trigger the wettability transition. As the track spacing further decreased, the neighboring track was totally wetted ($S = 4$ mm, Fig. 2d) due to a high

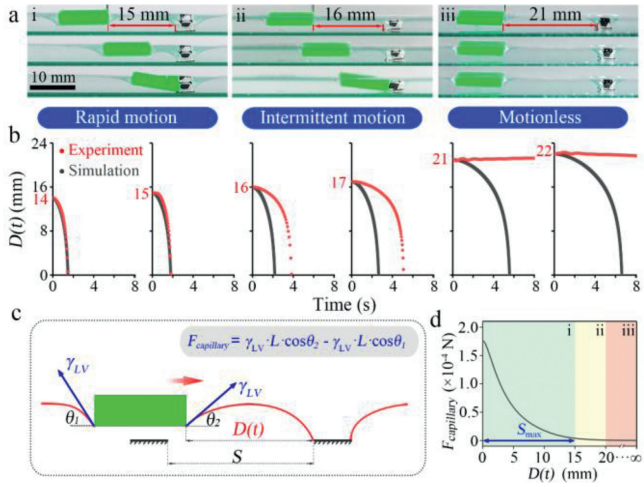

Fig. 3. (a) Three different motion states of PDMS with varied distance between PDMS and the track edge, $D(t_0)$. (b) Corresponding experimental (red dots) and simulated D(t) curves (gray dots) during the capillary transportation in (a). (c) Analysis of lateral capillary forces responsible for the capillary transportation. (d) The calculated $F_{capillary}$ *versus* $D(t)$.

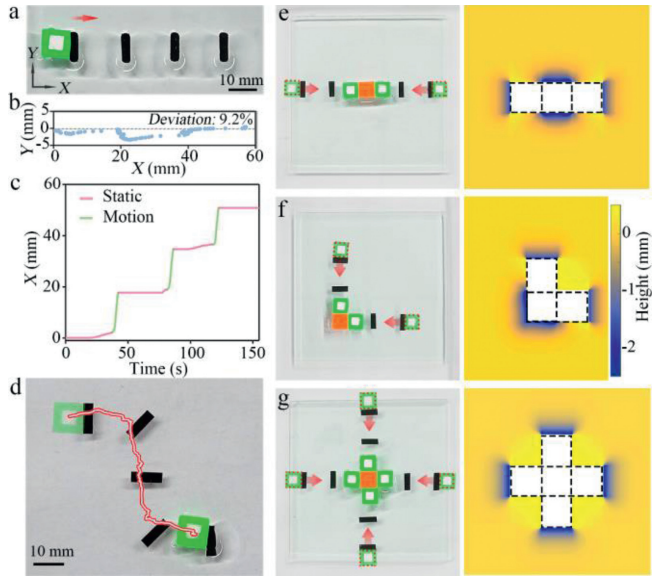

Fig. 4. (a) Photograph and (b) motion trajectories of the track-guided self-transportation of PDMS cuboid along a linear pathway. (c) The displacement of PDMS *versus* time curve in (a). (d) Track distribution to realize a designated motion along a curved pathway. Directed self-assembly to form a linear trimer (e), an L-shaped trimer (f), and a cross-shaped pentamer (g). The right columns of (e-g) are corresponding simulated results.

pH condition. Taken together, we determined S_{min} to be 6 mm to achieve selective wettability transition.

Furthermore, we have simulated the alkaline release and diffusion to calculate S_{min} by applying Fick's second law and finite element analysis (Fig. 2e and Section S4 in Supporting information). We calculated the spatiotemporal concentration distribution of hydroxyl ion, namely $C_{(OH^-)}$ (r, t), where r is the distance between the alkaline releasing source and the concerned positions, and t is the time interval after alkaline release. As the average time required to complete the wettability transition of the first track is roughly 38 s, we further took a sectional plane of $C_{(OH^-)}$ (r, $t = 38$ s) to study the spatial distribution of the released alkaline 'fuel' (Fig. 2g). The local $C_{(OH^-)}$ showed a sharp decay with an increased distance away from the alkaline releasing source. The critical distance (r) to reach the pH threshold was 9.3 mm, above which the next track could always keep superhydrophobic during the wettability transition process of the first track. Accordingly, the simulated value of S_{min} was 6.8 mm after considering the PDMS frame width of 2.5 mm (Fig. 2f). Thus, the simulated S_{min} matched well with the measured value.

The upper limit of the track spacing (S_{max}) remains to be determined, above which capillary force is insufficient for stable track-to-track transportation. To determine S_{max}, we have measured the critical interactive distance of capillary forces (Fig. 3a and Fig. S6 in Supporting information) by manually releasing the PDMS cuboid at a certain distance (14–22 mm) away from the track, followed by recording the motion processes with the real-time PDMS-track distance curves, namely D(t) curves (red dots in Fig. 3b). Additionally, we have quantified the lateral capillary force ($F_{capillary}$) *versus* $D(t)$ by force analyses with Eq. 1:

$$F_{capillary} = \gamma_{LV} \cdot L \cdot cos\theta_2 - \gamma_{LV} \cdot L \cdot cos\theta_1 \quad (1)$$

where γ_{LV} is the water surface tension, L is the wetted length (the PDMS side length), θ_1 and θ_2 are angles between the tangent direction of the menisci at the three-phase contact lines and the horizontal direction (Fig. 3c). The numerical results of $F_{capillary}$ *versus* $D(t)$ (Fig. 3d and Section S6 in Supporting information) have confirmed the declining trend with the increasing PDMS-track distance. Based on the integral of $F_{capillary}$ with respect to the motion distance, we obtained the decreasing free energy of the complete system (ΔU) as the interactive distance decreased (Fig. S9 in Supporting information), which exhibited the spontaneous tendency of energy dissipation during the capillary transportation. By further considering the resultant force of capillary attraction and fluid drag during transportation, we have calculated the theoretical D(t) curves (gray dots in Fig. 3b).

Based on the above measurement and calculations of capillary attraction between PDMS and tracks, we have observed three typical motion states (Figs. 3a and b). Besides the two expected states of rapid motion and motionless, a middle state of intermittent motion was observed. We attributed this phenomenon to inevitable interfacial disturbance [34]. Specifically, (i) when the track spacing $S \leq 15$ mm, it underwent a rapid motion in about 2 s to reach the next track, and the experimental $D(t)$ curves matched well with the calculated results. This motion behavior is caused by the strong lateral resultant force with a larger capillary attraction than fluid drag and random interfacial disturbance. (ii) When 16 mm $\leq S \leq 20$ mm, PDMS exhibited weak intermittent motions occasionally, leading to successful track-to-track transportation sometimes. In this distance range, the resultant force reduced down to a level comparable to the random interfacial disturbance, leading to the intermittent motion and the deviation between the experimental and simulated $D(t)$ curves. (iii) When $S > 20$ mm, we observed no motions at all (red dots in Fig. 3b) while theoretically capillary forces always exist to make transportation possible (gray dots in Fig. 3b). This result indicated that the lateral forces were insufficient to overcome the fluid drag and random interfacial disturbance. We further confirmed the presence of such random interfacial disturbance by observing the random trajectories of free-floating PDMS in a long time (Fig. S11 in Supporting information). Considering that the random interfacial disturbance is not favorable for stable transportation, we determined $S_{max} = 15$ mm to realize stable track-to-track transportation dominated by capillary attraction.

To verify the design principle of the above track spacing for track-to-track transportation, we have laid a linear path consisting of four tracks with a spacing of 15 mm between each other (Fig. 4a and Video S4 in Supporting information) and placed a PDMS near the first track. With alternate steps of wettability transition and capillary transportation, the PDMS underwent long-ranged self-

transportation, and the vertical deviation was about 9.2% because of slight adjustment during the wetting processes of the tracks (Fig. 4b). The time to complete one cycle of track-to-track motion was 39.7 ± 2.6 s, which include the two coupled processes of the static state of the wettability transition and the dynamic motion stage driven by capillary attraction (Fig. 4c). Besides linear motions, a curved pathway was also possible following the above design when the tracks were arranged in a curved form (Fig. 4d, Fig. S12 and Video S5 in Supporting information), owing to the error-tolerant advantage of precise alignment *via* long-ranged capillary forces [35].

Notably, the programmable feature of the above track-guided transportation mechanism is capable of directed self-assembly with on-demand design of spatial patterns. The trajectories could be facilely designed with designated PDMS number and pathways. Indeed, precise spatiotemporal control over multiple building blocks to achieve self-assembly of ordered structures, remains a challenge, which mainly relies on complex fabrication of building components and one-pot assembly without identifying individual components [36]. Herein, we took advantages of the track-guided transportation to regulate both the assembly path and the PDMS number for the formation of complex structures. We used a red PDMS with all four side surfaces modified as superhydrophobic as the targeted assembly position of the designated structure, and laid diverse tracks to realize the precise control over the transportation and assembly green PDMS.

As shown in Fig. 4e and Video S6 (Supporting information), two PDMS building blocks (colored with green) were released to approach the opposite sides of the targeted red PDMS under the guidance of the tracks. Both the building components of green PDMS and the targeted red PDMS were finally precisely aligned at the designate site. The design of the wettability conflicts between adjacent side surfaces of green PDMS contributed to precise local alignment following the principle of minimizing the interfacial free energy. The red PDMS with four superhydrophobic side surfaces provided 'assembly sites' from four directions, meaning the diversity of assembly patterns. With two pathways in the opposite directions, we obtained a linear trimer structure. By laying two pathways along the adjacent side surfaces of the red PDMS, an L-shaped trimer was automatically formed (Fig. 4f). When releasing four green PDMS building blocks from the four directions to approach the four side surfaces of the red PDMS, the self-assembly of a cross-shaped pentamer structure was realized through the directed self-assembly (Fig. 4g). The height of the water surface around the assemblies were simulated and the meniscus topology was visualized to indicate the interfacial free energy. Taken together, by changing the arrangement of guiding tracks, we could obtain designated assembly structures through directed self-assembly. Moreover, the tracks could be reused after acidic cleaning (Section S8 in Supporting information), allowing for repeated production of the designated assembly.

To summarize, we have developed a track-guided self-transportation system mediated by the sequential processes of wettability transition and capillary attraction. We used loaded alkali as the chemical fuel to trigger the selective wettability transition of pH-responsive tracks by studying the pH threshold to trigger the transition and the spatiotemporal alkaline distribution. With subtle designs of the track spacing, the selective wettability transition of the designated track was realized to change the meniscus of the track, which further exerted net lateral capillary forces onto PDMS for its track-to-track transportation. Furthermore, the pathway of the above track-guided transportation could be flexibly tailored and controlled, providing on-demand regulation of both the motion trajectories and time of individual building blocks. Such programmability was further applied to directed self-assembly to form designated structures. The above dynamic system has extended the applications of wettability transition, and provided a novel solution to programmable self-assembly, which is significant to advance the fundamental study of interfacial science and applications in semiconductor chip alignment [37], microrobot/swarm robots [38,39], programmable encoding [40], micromanufacturing [41] and metamaterials [42].

Declaration of competing interest

The authors declare that they have no known competing financial interests or personal relationships that could have appeared to influence the work reported in this paper.

Acknowledgments

This work was supported by the National Natural Science Foundation of China (Nos. 52122315, 21972008), Beijing Nova Program (No. Z201100006820021).

Supplementary materials

Supplementary material associated with this article can be found, in the online version, at doi:10.1016/j.cclet.2023.108538.

References

[1] M.J. Liu, S.T. Wang, L. Jiang, Nat. Rev. Mater. 2 (2017) 17036.
[2] F. Xia, L. Jiang, Adv. Mater. 20 (2008) 2842–2858.
[3] L.Y. Cui, Y. Yan, X.Y. Zhao, et al., Chin. Chem. Lett. 28 (2017) 1–5.
[4] J. Lahann, S. Mitragotri, T.N. Tran, et al., Science 299 (2003) 371–374.
[5] X.J. Feng, L. Feng, M.H. Jin, et al., J. Am. Chem. Soc. 126 (2004) 62–63.
[6] F. Xia, L. Feng, S.T. Wang, et al., Adv. Mater. 18 (2006) 432–436.
[7] Y. Jiang, Y.J. Yin, X.C. Zha, X.Q. Dou, C.L. Feng, Chin. Chem. Lett. 28 (2017) 813–817.
[8] L.P. Wen, Y. Tian, L. Jiang, Angew. Chem. Int. Ed. 54 (2015) 3387–3399.
[9] G. Huang, X.H. Song, Y.Y. Chen, et al., Chin. Chem. Lett. 31 (2020) 1839–1842.
[10] S.T. Wang, Y.L. Song, L. Jiang, J. Photochem. Photobiol. C 8 (2007) 18–29.
[11] D.L. Tian, X.F. Zhang, Y. Tian, et al., J. Mater. Chem. 22 (2012) 19652–19657.
[12] R.X. Qu, Y.N. Liu, W.F. Zhang, et al., Chem. Sci. 10 (2019) 4089–4096.
[13] G.N. Ju, M.J. Cheng, M. Xiao, et al., Adv. Mater. 25 (2013) 2915–2919.
[14] S.F. Mao, X.H. Hu, Y.M. Tanaka, et al., Chin. Chem. Lett. 33 (2022) 3083–3086.
[15] F.J. Chen, W. Xiang, S.H. Yin, S. Huang, ACS Appl. Mater. Interfaces 13 (2021) 20885–20896.
[16] M. Wang, L. Zhou, Y.Q. Hou, et al., Chin. Chem. Lett. 31 (2020) 1914–1918.
[17] X. Zheng, Z.Y. Gao, D.L. Tian, X.F. Zhang, L. Jiang, Adv. Mater. Interfaces 3 (2016) 1600461.
[18] F.T. Liu, Q.M. Pan, J. Mater. Chem. A 6 (2018) 11288–11295.
[19] M. Xiao, X.P. Gao, M.J. Cheng, et al., Small 10 (2014) 859–865.
[20] Z. Dang, L.B. Liu, Y. Li, Y. Xiang, G.L. Guo, ACS Appl. Mater. Interfaces 8 (2016) 31281–31288.
[21] Y.H. Sun, Z.G. Guo, Adv. Mater. 32 (2020) 2004875.
[22] X.T. Zhao, Y.Y. Jiang, L.J. Cheng, et al., Chin. Chem. Lett. 33 (2022) 3859–3864.
[23] X.Y. Li, J.J. Liu, R.X. Qu, et al., Nat. Commun. 12 (2021) 80.
[24] J. Wang, W. Gao, H. Zhang, et al., Sci. Adv. 4 (2018) eaat7392.
[25] L.N. Zhang, M.M. Song, M. Xiao, F. Shi, Adv. Funct. Mater. 26 (2016) 851–856.
[26] M.M. Song, M.J. Cheng, G.N. Ju, Y.J. Zhang, F. Shi, Adv. Mater. 26 (2014) 7059–7063.
[27] R.X. Qu, X.Y. Li, Y.N. Liu, et al., Angew. Chem. Int. Ed. 59 (2020) 13437–13443.
[28] Y.M. Zhang, Y.H. Han, X.L. Ji, et al., Nature 610 (2022) 74–80.
[29] M.J. Cheng, L.N. Zhang, F. Shi, Mater. Chem. Front. 5 (2021) 129–150.
[30] S.T. Wang, K.S. Liu, X. Yao, L. Jiang, Chem. Rev. 115 (2015) 8230–8293.
[31] M. Xiao, T.M. Xian, F. Shi, Angew. Chem. Int. Ed. 54 (2015) 8952–8956.
[32] M.J. Cheng, G.Q. Zhu, L. Li, et al., Angew. Chem. Int. Ed. 57 (2018) 14106–14110.
[33] P. Peruzzo, A. Define, H. Nepf, Water Resour. Res. 48 (2012) W07512.
[34] I. Ho, G. Pucci, D.M. Harris, Phys. Rev. Lett. 123 (2019) 254502.
[35] M.H. Tan, P. Tian, Q. Zhang, et al., Nat. Commun. 13 (2022) 5201.
[36] L. Cademartiri, K.J.M. Bishop, Nat. Mater. 14 (2015) 2–9.
[37] R.J. Knuesel, H.O. Jacobs, Proc. Natl. Acad. Sci. U. S. A. 107 (2010) 993–998.
[38] M.Z. Miskin, A.J. Cortese, K. Dorsey, et al., Nature 584 (2020) 557–561.
[39] M. Rubenstein, A. Cornejo, R. Nagpal, Science 345 (2014) 795–799.
[40] X.F. Ji, R.T. Wu, L.L. Long, et al., Adv. Mater. 30 (2018) 1705480.
[41] L.L. Ong, N. Hanikel, O.K. Yaghi, et al., Nature 552 (2017) 72–77.
[42] C. Coulais, E. Teomy, K. Reus, et al., Nature 535 (2016) 529–532.